Article

Effects of Nanocomposite Derivatives of Ni−Fe, Ni−Co, Ni−Co−Fe Prussian Blue Analogues on the Thermal Decomposition Performance of Nitrocellulose

Junhong Liu, Zhitao Liu,* Jing Yang, Bin Xu, Feiyun Chen, and Xin Liao

Read Online

ACCESS | Metrics & More | Article Recommendations

ABSTRACT: The incorporation of nanomaterials generated from Prussian blue (PB) derivatives has emerged as a promising strategy to significantly improve the properties of energetic materials. In this study, we comprehensively investigated the influence of nanomaterials derived from PB on the thermal decomposition characteristics of energetic materials. To achieve this goal, we prepared nanomaterials using coprecipitation and heat treatment methods with PB derivatives as catalysts. Advanced techniques such as X-ray diffraction, scanning electron microscopy, transmission electron microscopy, Brunauer−Emmett−Teller (BET) analysis for specific surface area and pore size, and X-ray photoelectron spectroscopy were employed to thoroughly characterize these nanomaterials. Differential scanning calorimetry was used to assess the thermal behavior of nitrocellulose (NC), and the relevant kinetic parameters were determined through thermal decomposition kinetics calculations and analysis. This work revealed the influence of catalysts on the NC decomposition process and provided comprehensive insights into the effect of integrating nanomaterials derived from PB derivatives on the thermal decomposition performance of NC. The results of this work demonstrated the possibility of using nanomaterials generated from PB derivatives as effective catalysts to enhance the thermal decomposition characteristics of NC, offering interesting opportunities for their application in the field of high-energy materials.
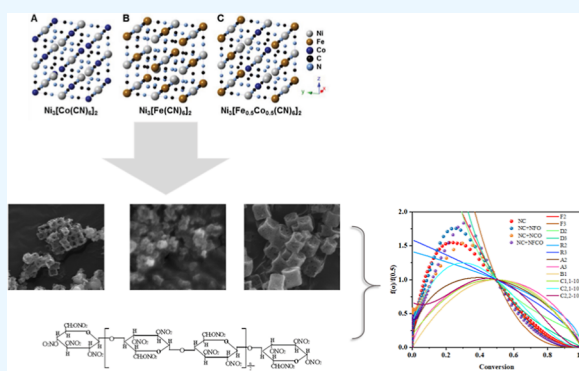
1. INTRODUCTION

A common element in creating smokeless powders, blasting gelatin, dynamite, single-base and double-base guns, and rocket propellants is nitrocellulose (NC).[1] The thermal properties of NC have been extensively studied. Wang[2] studied the thermal decomposition process of NC. Zhang[3] investigated the effect of graphene oxide nanocomposites on the stability of NC.

Extensive research efforts have been dedicated to revealing the thermal decomposition characteristics of NC. Under ambient conditions, NC exhibits gradual degradation, while significant decomposition occurs within the temperature range of 70 to 160 °C.[4] High-molecular-weight NC molecules decompose in the solid phase without melting during this heterogeneous reaction-based breakdown process. Hu Rongzu has meticulously investigated to better understand the complex self-catalyzed reaction kinetics of NC,[5] employing thermal analysis techniques. Furthermore, researchers such as Ning[6] and Pan Qing have employed a synergistic approach, combining Fourier-transform infrared spectroscopy and thermal analysis techniques, to delve into the denigration reaction kinetics of high-nitrogen content NC. Their efforts have also shed light on the influence of lead−copper complexes on the thermal decomposition process of NC. Additionally,

Wei's[7] researched the effects of nanometal oxides on NC in an attempt to understand their effects on the thermal decomposition performance of NC.

Prussian blue (PB), as a typical metal−organic framework (MOF) material, has received wide attention in recent years due to its low cost, simple preparation process, and unique hollow framework structure.[8,9] Using these advantages, PB-derived nanomaterials gain distinctive qualities that make them highly desirable in a range of applications. In particular, nanocatalysts, due to their small particle size, large surface area, and high catalytic activity, have become a hot topic in explosive research.[10−12] MOFs can form in situ metal (metal oxide)−carbon-based complexes with combustion catalytic activity during the combustion process of explosives.[13] However, the combustion process is inherently uncontrollable, making it difficult to control the structural characteristics of the formed
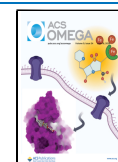
catalysts and adjust their catalytic activity. If MOFs are transformed into their derivatives through controlled reaction methods before use, apart from whether a new type of combustion catalyst is obtained, the microstructure of the catalysts can also be effectively regulated, which is advantageous for studying their structure—activity relationships.[14,15] Prior to use, MOFs can be converted into their derivatives through controlled reaction methods. This not only enables the production of a new type of combustion catalyst but also allows for effective regulation of the catalyst's microstructure, which is advantageous for studying its structure—activity relationship.

In summary, PB is a multifunctional and highly demanded MOF material, and the synthesis of nanomaterials based on PB creates interesting new opportunities for high-energy formulations.[16] With the current research exploration and utilization of the unique properties of PB-derived nanomaterials, the fields of explosives and fireworks are expected to experience significant progress and innovation.[17] Ultimately, this will enhance key applications in national security and other fields.[18−20]

There is currently a dearth of study on the catalytic behavior and catalytic breakdown processes of other energetic molecules, with the majority of studies on MOF-based combustion catalysts concentrating on their catalytic effects on ammonium perchlorate propellants.[21] This work offers a novel solution in response: PB analogues were created using Ni—Fe, Ni—Co, and Ni—Fe—Co metals, and the resulting compounds were then incorporated into NC as nanocatalysts. We conducted a thorough investigation into how these loaded nanocomposite metal oxides affected the thermal deterioration of NC, and we produced valuable data to direct future application-focused research.

2. EXPERIMENTAL SECTION

2.1. Reagents. The types, purities, and manufacturers of the chemical reagents used in this paper are shown in Table 1.

Table 1. Reagents Utilized in the Synthesis Process

reagent	purity	manufacturer
nickel nitrate hexahydrate	AR	Guangdong Xi Long Scientific Co., Ltd
cobalt nitrate hexahydrate	AR	Guangdong Xi Long Scientific Co., Ltd
potassium hexacyanoferrate (III) ate	AR	Shanghai Bide Pharmaceutical Co., Ltd
cobalt(II) potassium cyanide	AR	Shanghai Aladdin Reagent Co., Ltd
potassium nickel tetra cyanate	AR	Shanghai Macklin Biochemical Co., Ltd
sodium citrate	AR	Shanghai Aladdin Reagent Co., Ltd

2.2. Experimental Instruments. The following instruments were used: FEI Company Quanta 250 scanning electron microscope from the United States; test voltage: 10 kV.

TA Company TGA 550 thermogravimetric analyzer, temperature range 50−800 °C, alumina crucible, sample mass of about 2 mg, air flow of 20 mL min^{-1}.

Nikaku smartlab9 equipped with an ultrahigh speed detector X-ray diffractometer, which uses copper target K-α ray with a wavelength of 1.54178 Å to scan the sample and the scanning Angle range of 10−80°.

X-ray photoelectron spectroscopy (XPS) measurements were made on an ESCALAB 250Xi spectrometer (Thermo Scientific, USA) equipped with a 30 eV pass-through energy, 100 W (10 kV and 10 mA), monochromatized Al Kα X-ray ($h\nu$ = 1486.65 eV) source. All samples were analyzed at pressures less than 1.0×10^{-9} Pa. The spectrum was obtained by the advantage software (Version 5.979) with a step size of 0.05 eV.

The non-isothermal differential scanning calorimetry (DSC) measurements of the samples were carried out by the Nesch DSC 204 F1 instrument. A stainless steel high-pressure crucible, using a covered alumina crucible with a small (needle-sized) hole in the center as an open environment, refers to the gas produced by the thermal decomposition of the sample that can escape from the crucible. The sample mass is about 0.6 mg. The scavenging gas and the protection gas were nitrogen, and the flow rates were 40 and 60 mL min^{-1}, respectively. The samples were tested by DSC at heating rates of 1, 2, 5, and 10 °C min^{-1}, in the temperature range of 50.0−300.0 °C.

2.3. Synthesis of Prussia Blue Analogues (Ni Fe-PBA, Ni Co-PBA, Ni−Co Fe-PBA). The nanocubes of PB analogues, including Ni and Fe (NF-PBA), Ni and Co (NC-PBA), and Ni, Fe, and Co (NFC-PBA) precursors, were synthesized using a coprecipitation method. For the synthesis of NF-PBA, 200 mL of deionized water was used to dissolve 6 mmol of nickel nitrate, 9 mmol of sodium citrate, and 4 mmol of potassium ferricyanide (III) in a separate 200 mL of deionized water. After mixing the two solutions, they were allowed to sit at room temperature. The creation of uniformly distributed precursor nanoparticles was caused by the effective inhibition of precipitation processes by citrate ions. The upper clear solution was decanted after a predetermined amount of reaction time, and the bottom white powder was collected. The powder was then extensively mixed with anhydrous ethanol to act as a dispersant, and the mixture was then centrifuged to collect the powder. This process was repeated several times until the washing centrifugation was completed. Finally, the powder was dried in a vacuum oven for 12 h to obtain the nanocubes containing Ni and Fe (NF-PBA).[22]

The same procedure was used to make NC-PBA and NFC-PBA nanocubes; however, for NC-PBA, potassium ferricyanide in NF-PBA was swapped out for a 4 mmol solution of potassium hexacyanocobaltate (III). A mixture of 2 mmol of hydrated nickel nitrate, 6 mmol of potassium hexacyanocobaltate (II), and 5.14 mol of potassium hexacyanoferrate (III) was employed to create NFC-PBA.

2.4. Synthesis of PB Oxide Composites. After synthesizing the precursors, a crucial step involves subjecting the precursors to a thermal treatment process.[23,24] By oxidizing the metal ions to increase the catalytic activity, this procedure attempts to enable the escape of organic ligands from the MOF and produce pores within the structure. However, it should be noted that the thermal treatment's duration and heating temperature have a significant impact on the final product's shape and structure.

This work involved heat treatment of the Ni−Fe PBA precursor in an ambient air environment. Through this process, the cyanide groups in the MOF oxidize to produce carbon dioxide and nitrogen dioxide, which increases the specific surface area and creates holes. Consequently, the material's catalytic performance is improved. Ni−Co PBA and Ni−Fe−Co PBA precursors can also be thermally treated to increase their catalytic performance while keeping their original

framework architectures. It is feasible to maximize the attributes of the final product, enabling increased catalytic activity and pore creation, by precisely regulating the heating temperature and length of the thermal treatment process.[25,26]

3. RESULTS AND DISCUSSION

3.1. Analysis of a Mass Change of Precursor during Calcination. The precursors Ni−Fe PBA, Ni−Co PBA, and Ni−Fe−Co PBA were all employed in this experiment, and they all received thermal treatment in an environment of outside air.[27,28] The cyanide groups in the MOF were oxidized during this reaction, generating carbon dioxide and nitrogen dioxide. While simultaneously adding pores to the material, the original framework structure was preserved, increasing the specific surface area. As a result, the materials' catalytic performance was greatly improved.

In Figure 1, sample 1 represents $Ni_3[Fe(CN)_6]_2$, sample 2 represents $Ni_3[Co(CN)_6]_2$, and sample 3 represents $Ni_3[FeCo(CN)_6]_2$. From Figure 1a, it can be observed that sample 1 ($Ni_3[Fe(CN)_6]_2$) undergoes four distinct decomposition stages when heated in an air atmosphere. The first-step weight loss of 21.4% is caused by the evaporation of adsorbed water molecules present in the precursor and takes place between 100 and 200 °C. The weight loss of 7.49% that results from the second stage, which takes place between 250 and 300 °C, is predominantly caused by the evaporation of crystalline water that is present in between $Ni_3[Fe(CN)_6]_2$ molecules. The third stage takes place between 320 and 370 °C, and a weight reduction of 10.35% is the outcome. A weight loss of 11.28% happens in the fourth stage, which takes place between 400 and 650 °C. After 400 °C, the weight continues to decrease, indicating a progressive oxidation of the interiors of the particles above 400 °C and partial disintegration of the precursor between 320 and 370 °C. The curve eventually levels off around 600 °C, signifying stabilization. Equation 1 represents the reaction equation for the thermal decomposition of $Ni_3[Fe(CN)_6]_2$ in the air atmosphere

$$Ni_3[Fe(CN)_6]_2 + O_2 \rightarrow NiO + Fe_3O_4 + CO_2 + NO_2 \tag{1}$$
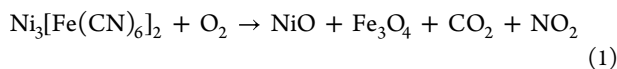
Sample 2 is the precursor $Ni_3[Co(CN)_6]_2$, and Figure 1b shows that when heated in an air atmosphere, the sample 2 precursor passes through two different stages of breakdown. The first step occurs between 100 to 200 °C, resulting in a weight loss of 22.94%, attributed to the evaporation of adsorbed water molecules present in the precursor. The second step occurs between 250 to 350 °C, leading to a weight loss of 28.29%, indicating the oxidation of cyanide groups within the $Ni_3[Co(CN)_6]_2$ MOF into carbon dioxide and nitrogen dioxide. Beyond 350 °C, the weight continues to decrease, suggesting incomplete decomposition of the precursor between 250 and 350 °C, and gradual oxidation of the particles' interiors after 350 °C. The curve levels off at 600 °C, indicating stabilization. Equation 2 represents the reaction equation for the thermal decomposition of $Ni_3[Co(CN)_6]_2$ in the air atmosphere

$$Ni_3[Co(CN)_6]_2 + O_2 \rightarrow NiO + Co_3O_4 + CO_2 + NO_2 \tag{2}$$
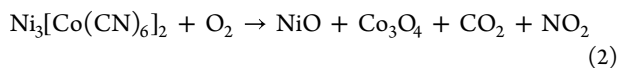
Sample 3 represents the $Ni_3[Fe_{0.5}Co_{0.5}(CN)_6]_2$ precursor, and from Figure 1c, it can be observed that sample 3 precursor undergoes two distinct decomposition stages when heated in an air atmosphere. The first step occurs between 100 to 200
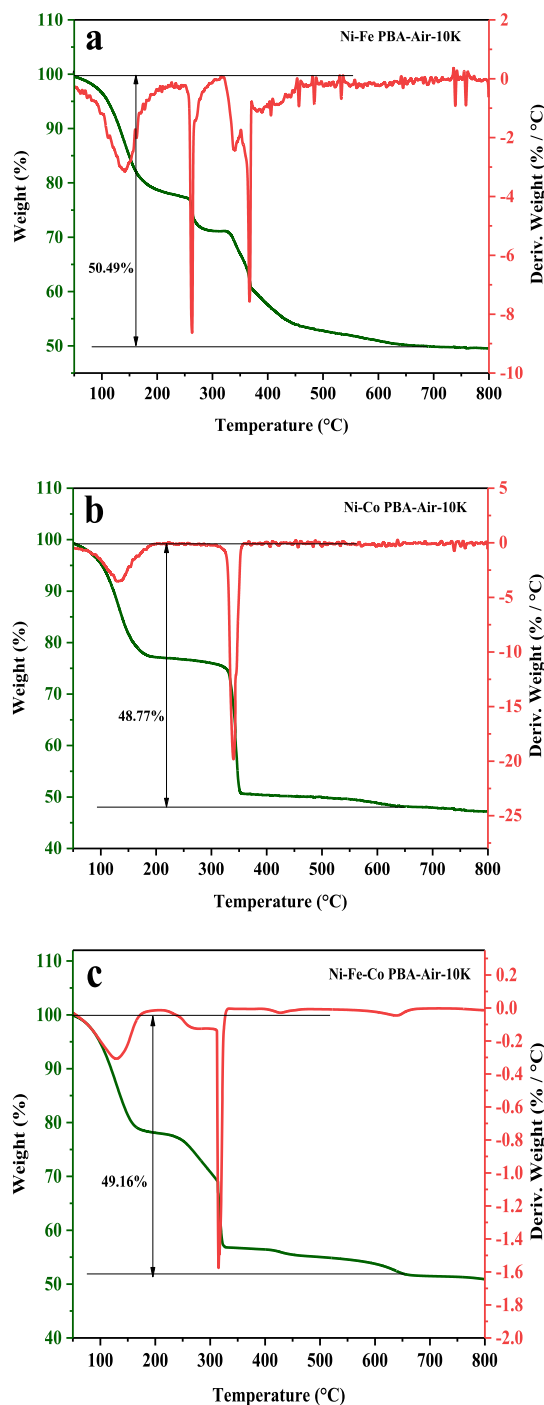

Figure 1. $Ni_3[Fe(CN)_6]_2$ (a), $Ni_3[Co(CN)_6]_2$ (b), $Ni_3[Fe_{0.5}Co_{0.5}(CN)_6]_2$ (c) of TG and DTG curves heated in an air atmosphere.

°C, resulting in a weight loss of 22.01%, attributed to the evaporation of adsorbed water molecules present in the precursor. The second step occurs between 250 and 350 °C, leading to a weight loss of 27.15%, indicating the oxidation of cyanide groups within the $Ni_3[Fe_{0.5}Co_{0.5}(CN)_6]_2$ MOF into carbon dioxide and nitrogen dioxide. Beyond 350 °C, the weight continues to decrease, suggesting incomplete decomposition of the precursor between 250 and 350 °C and gradual oxidation of the particles' interiors after 350 °C. The curve levels off at 600 °C, indicating stabilization. Equation 3

represents the reaction equation for the thermal decomposition of $Ni_3[Fe_{0.5}Co_{0.5}(CN)_6]_2$ in the air atmosphere

$$Ni_3[Fe_{0.5}Co_{0.5}(CN)_6]_2 + O_2$$
$$\rightarrow NiO + Fe_3O_4 + Co_3O_4 + CO_2 + NO_2 \qquad (3)$$
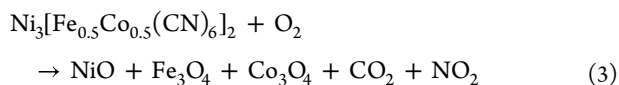
According to the thermogravimetric data, the calcination temperature of Ni−Fe PBA, Ni−Co PBA, and Ni−Fe−Co PBA precursors was chosen at 600 °C under an air atmosphere.

3.2. Analysis of Catalyst Surface Morphology.
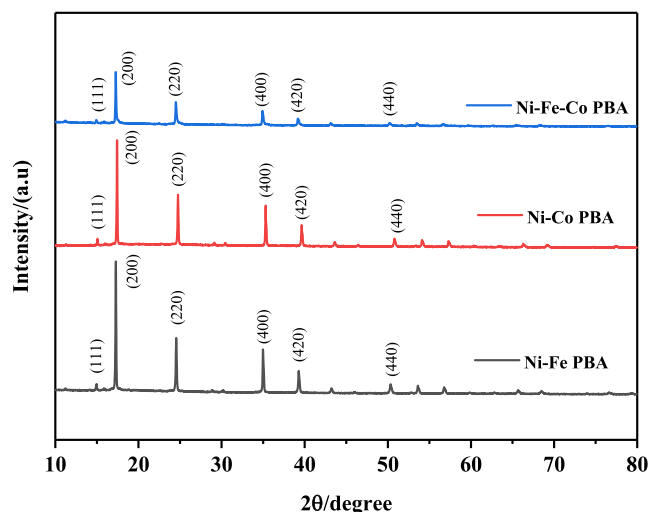*3.2.1. XRD of NF-PBA, NC-PBA, and NFC-PBA.* Figure 2

Figure 2. XRD curves of Ni−Fe PBA, Ni−Co PBA, and Ni−Fe−Co PBA.

shows the crystal structure of the precursor of NF-PBA, NC-PBA, and NFC-PBA, which is consistent with the standard diffraction card of $Ni_3[Fe(CN)_6]_2 \cdot 10H_2O$, $Ni_3[Co(CN)_6]_2 \cdot 3H_2O$, $Ni_3[Fe_{0.5}Co_{0.5}(CN)_6]_2 \cdot 10H_2O$ (JCPDS 46-0906, JCPDS 22-1184, JCPDS 46-0906).[22]

3.2.2. SEM and TEM Characterization of NF-PBA, NC-PBA, and NFC-PBA. The SEM pictures of the precursors and calcined products are displayed in Figure 3. NF-PBA, NC-PBA, and NFC-PBA are represented by Figure 3a−c, in that order. The pictures show that the PB equivalents of several metals have cubic structures. Of these, the average size of the nanocube structures shown by NF-PBA is 180 nm, the average size of the nanocube structures shown by NC-PBA is roughly 300 nm, and the average size of the nanocubes shown by NFC-PBA is 400 nm. NF-PBA following high-temperature calcination at 600 °C is depicted in Figure 3d,g. The calcined product exhibits severe aggregation, a rougher surface, and altered overall morphology with irregular forms and an average size of 80 nm. The cubic structure is virtually preserved when combined with the TEM image shown in Figure 3j. The lattice spacing of 0.24 nm corresponds to either the (111) plane of NiO or the (311) plane of Fe_3O_4.[29]

The −CN group in NC-PBA is oxidized during the calcination process, leaving behind metal oxides that constitute the general framework. The calcined product of NC-PBA shows a hollow cubic framework structure with an average size of 200 nm, as shown in Figure 3e,h. It is evident from Figure 3k that the result is made up of fragment connections that form

a polygonal structure inside the cubic framework, and the 0.46 nm lattice spacing is in line with the Co_3O_4 (111) plane.

Similar to this, metal oxides are still present in NFC-PBA following the oxidation of the cyanide groups during air calcination. Small pores are seen on the NFC-PBA surface (Figure 3f,i), which largely preserves the 270 nm-average cubic structure. The SEM image and Figure 3l demonstrate the preservation of the cubic structure of nickel−iron−cobalt oxides, with a lattice spacing of 0.24 nm corresponding to the (111) plane of NiO or the (311) plane of Fe_3O_4.

Figure 4 shows the FT-IR spectrum of the PB analogues after calcination. It can be seen from the figure that the products after calcination did not show a strong absorption peak between 2000 and 2200 cm^{-1}, and it can be concluded that the cyanogen exercise of PB analogues during calcination eventually transformed into a composite oxide catalyst.

3.2.3. XPS Analysis of Different Catalysts. 3.2.3.1. XPS Analysis of NFO. Figure 5 shows the XPS analysis of the NFO (Ni−Fe PBA) nanocube catalyst, which further validates the specific composition of the calcined products and the elemental valence states. In the Ni 2p3/2 region of the XPS spectrum (Figure 5a), the main peak with a binding energy of 853.7 eV is attributed to NiO (II). Two satellite peaks are observed at binding energies of 878.5 and 860.48 eV, respectively. These satellite peaks indicate the presence of Ni 2p3/2 in a different chemical environment. Furthermore, in Figure 5b, peaks at binding energies of 710.78 and 713.18 eV indicate the coexistence of Fe (II) and Fe (III) species. The XPS results confirm the presence of Fe_3O_4 in the Ni−Fe composite oxide. The O 1s peak can be deconvoluted into three components, namely, C−O, MOx (M = Ni, Fe), and C=O, as shown in Figure 5c. The oxygen component mainly originates from the metal oxides present in the Ni−Fe composite, providing clear evidence that the Ni−Fe composite oxide consists of NiO and Fe_3O_4 components.

3.2.3.2. XPS Analysis of NC-PBA. The XPS spectra of Ni 2p is shown in Figure 6a. Following peak analysis, distinctive peaks belonging to Ni^{2+} are found. Ni^{2+} 2p3/2 orbitals are represented by the binding energy of 853.7 eV, whereas Ni^{2+} 2p1/2 orbitals are represented by the binding energy of 871.87 eV. The peaks at 860.4 and 878.8 eV are satellite peaks associated with the Ni^{2+} 2p3/2 and 2p1/2 orbitals, respectively. In Figure 6b, the XPS spectrum of Co 2p is shown, and after peak analysis, two pairs of characteristic peaks for Co^{3+} and Co^{2+} are observed. The binding energy of 781.2 eV corresponds to the Co^{3+} 2p3/2 orbital, while the binding energies of 781.5 and 797 eV correspond to the Co^{2+} 2p3/2 and 2p1/2 orbitals, respectively. The peak at 785.6 eV is a satellite peak associated with Co^{2+}. The XPS spectrum of O 1s is shown in Figure 6c, and following peak analysis, the distinctive oxygen peaks in metal oxides are found. The oxygen in metal oxides is represented by the peak at 529.2 eV. Furthermore, it is further confirmed that the calcined product is a mixture of NiO and Co_3O_4 by assigning the peaks at 532.4 and 530.6 eV to Co_3O_4 and NiO_2, respectively.

3.2.3.3. XPS Analysis of NCF-PBA. The complete spectrum is shown in Figure 7e, which verifies that the NFCO compound contains the elements Ni, Fe, Co, and O. The XPS spectra of Ni 2p are displayed in Figure 6a. Following peak analysis, distinctive peaks belonging to Ni^{2+} are found. The Ni^{2+} 2p3/2 orbital has a binding energy of 853.7 eV, whereas the Ni^{2+} 2p1/2 orbital has a binding energy of 871.87 eV. Satellite peaks linked to the Ni^{2+} 2p3/2 and 2p1/2 orbitals,
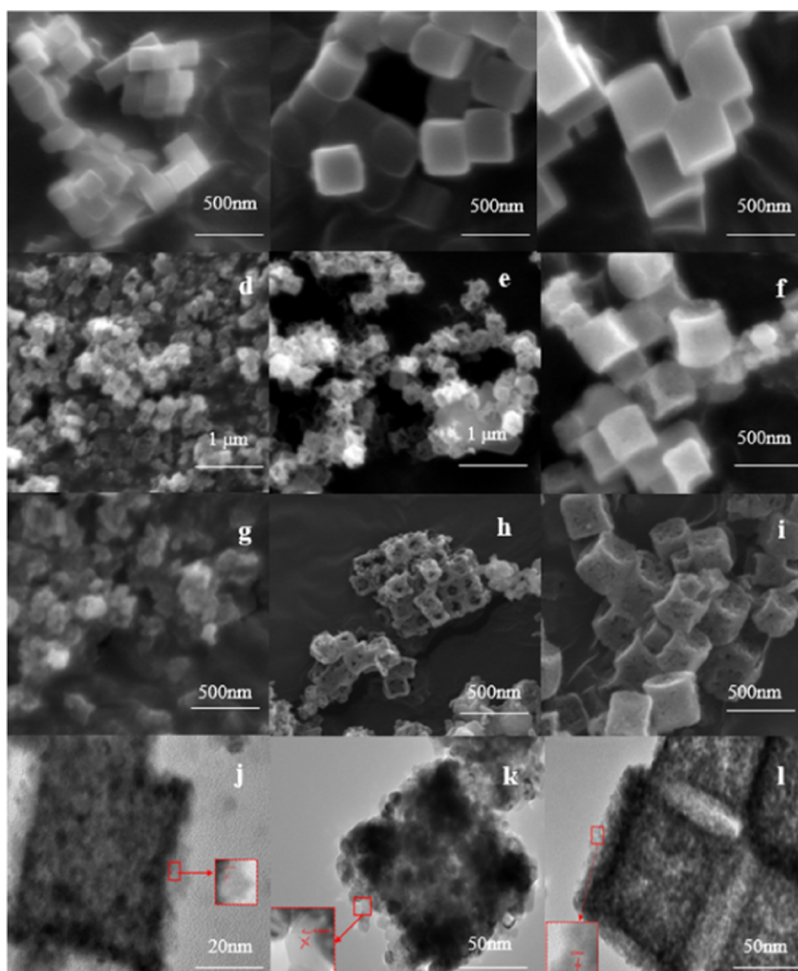
Figure 3. SEM images of NF-PBA (a), NC-PBA (b), NFC-PBA (c), and the calcined products at 600 °C (d–i). The TEM images of the calcined products are shown in (j–l).
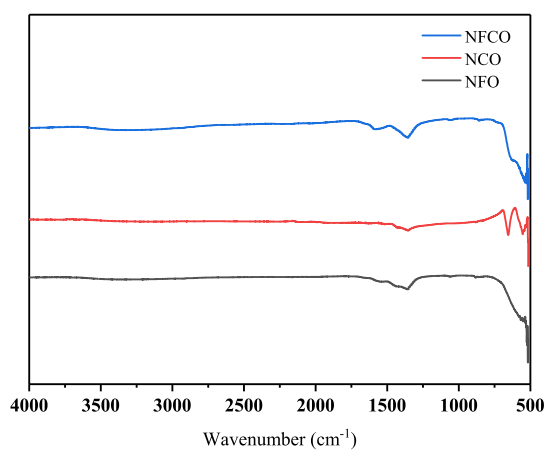

Figure 4. FT-IR of PB derivatives.

Figure 5. Full spectrum XPS spectra of (a) Ni 2p, (b) Fe 2p, (c) O 1s, and (d) of NFO.

respectively, are located at 860.4 and 878.8 eV. Figure 6b displays the XPS spectrum of Fe 2p, and after peak analysis, characteristic peaks of Fe^{2+} are observed. The peaks at 709.68 and 712.65 eV indicate the presence of Fe(II) and Fe(III), respectively, clearly indicating the existence of Fe_3O_4 in the Ni−Fe−Co composite oxide. In Figure 7c, the binding energy of 781.2 eV corresponds to the Co^{3+} 2p3/2 orbital, while the binding energies of 781.5 and 797 eV correspond to the Co^{2+}
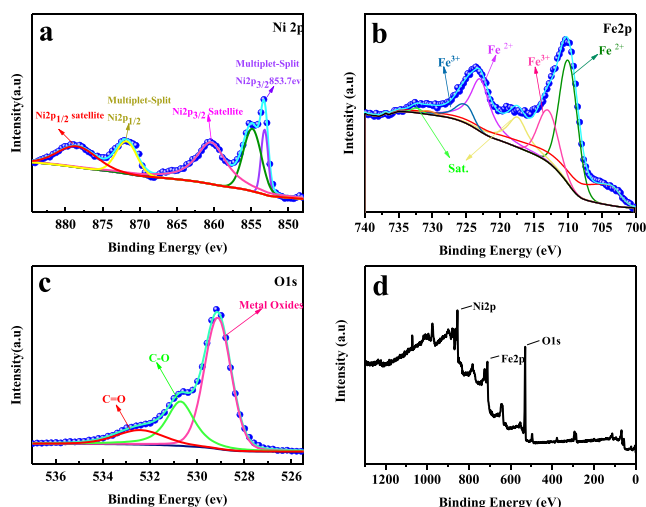
2p3/2 and 2p1/2 orbitals, respectively. The peak at 785.6 eV is identified as a satellite peak (labeled as "shake-up"). Figure 7d shows the XPS spectrum of O 1s, and the peak at 529.2 eV corresponds to oxygen in metal oxides. This additional evidence that NiO, Fe_3O_4, and Co_3O_4 make up NFCO
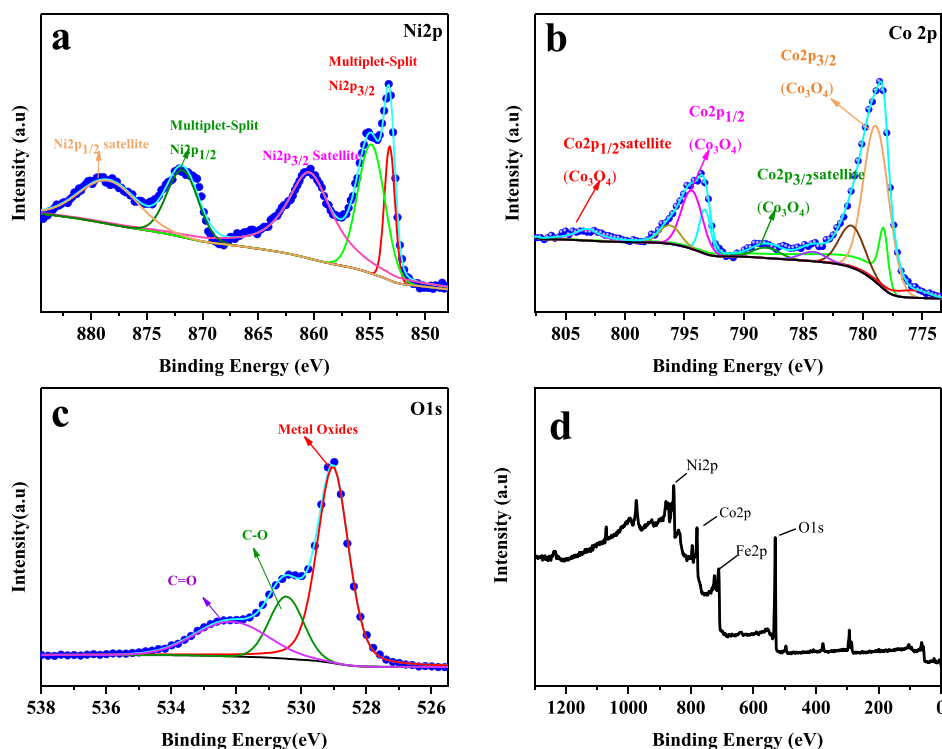
Figure 6. Full spectrum XPS spectra of (a) Ni 2p, (b) Co 2p, (c) O 1s, and (d) of NCO.

comes from the metal oxides found in the Ni−Fe composite oxide.

3.2.4. BET Test and Analysis of Nanocomposite Oxides. By analyzing the N_2 physical adsorption−desorption isotherms at 77 K, the specific surface area and pore structure of PB derivative materials treated at different temperatures can be determined. It can be observed that the adsorption−desorption isotherms of nickel−iron nanocomposite oxides belong to Type II (Figure 8a), indicating the presence of abundant mesoporous structures in nickel−iron nanocomposite oxides, making them typical mesoporous materials with a BET surface area of 26.40 m^2/g. The pore size distribution calculated using the Horvath−Kawazoe method for testing specific surface area adsorption is mainly concentrated around 24.22 nm, with a pore volume of 0.18 cm^3/g (Table 2). Combining the SEM images of nickel−iron PB derivatives in Figure 3d,g, it can be inferred that the nanocomposite oxide materials exhibit partial connectivity fractures and local structural collapse, while fragments of the connectivity fill the pores.

Similarly, the adsorption−desorption isotherms of nickel−cobalt nanocomposite oxides also belong to Type II (Figure 8b), indicating the presence of abundant mesoporous structures in nickel−cobalt nanocomposite oxides, making them typical mesoporous materials with a BET surface area of 19.63 m^2/g. The pore size distribution calculated using the Horvath−Kawazoe method for testing specific surface area adsorption is mainly concentrated around 26.16 nm, with a pore volume of 0.085 cm^3/g (Table 3).

The adsorption−desorption isotherms of nickel−iron-cobalt nanocomposite oxides also belong to Type II (Figure 8c), indicating the presence of abundant mesoporous structures in nickel−iron-cobalt nanocomposite oxides, making them typical mesoporous materials with a BET surface area of 23.52 m^2/g. The pore size distribution calculated using the Horvath−Kawazoe method for testing specific surface area adsorption is

mainly concentrated around 19.52 nm, with a pore volume of 0.12 cm^3/g (Table 3).

3.3. Effect of Ni−Co, Ni−Fe, Ni−Fe−Co Metal Oxide Catalysts on the Decomposition Kinetics of NC. *3.3.1. NC Dynamic DSC Analysis of Different Catalyst Loads.* At a heating rate of 10 K/min, Figure 9 displays the dynamic DSC curves of NC loaded with various catalysts (nanocomposite oxides/NC in a 1:4 ratio), with the pertinent values given in Table 3. Catalysts designed to enhance detonation performance ought to have the least possible effect on the material's thermal stability. From Table 3, it can be observed that these catalysts all have some influence on the decomposition of NC. The starting decomposition temperature of NC is 197.4 °C, the exothermic peak temperature is 207.8 °C, and the termination temperature is 225.4 °C. After the addition of catalysts NFO, NCO, and NFCO, the starting decomposition temperatures are advanced by 2, 0.7, and 0.5 °C, respectively. The peak temperatures are advanced by 2.5, 4.5, and 5.3 °C. The termination temperatures are advanced by 7.6, 11.6, and 14.8 °C. The decomposition temperature ranges are 28.0, 22.4, 17.1, and 13.7 °C. This indicates that under the conditions of catalyst loading, the thermal stability of the mixed system of NC is slightly reduced, but the impact on the decomposition of NC is relatively small.

3.3.2. Decomposition Dynamics Analysis Based on a Model-Free Method. In the kinetic methods used in the field of thermal analysis, it is generally accepted that the reaction rate is only a function of temperature T and conversion α

$$\frac{d\alpha}{dt} = k(T)f(\alpha) \tag{4}$$

where α is the conversion rate, t is the time, k is the reaction rate constant, which can be expressed by the Arrhenius formula (eq 5), and $f(\alpha)$ is the mechanism function.[30]
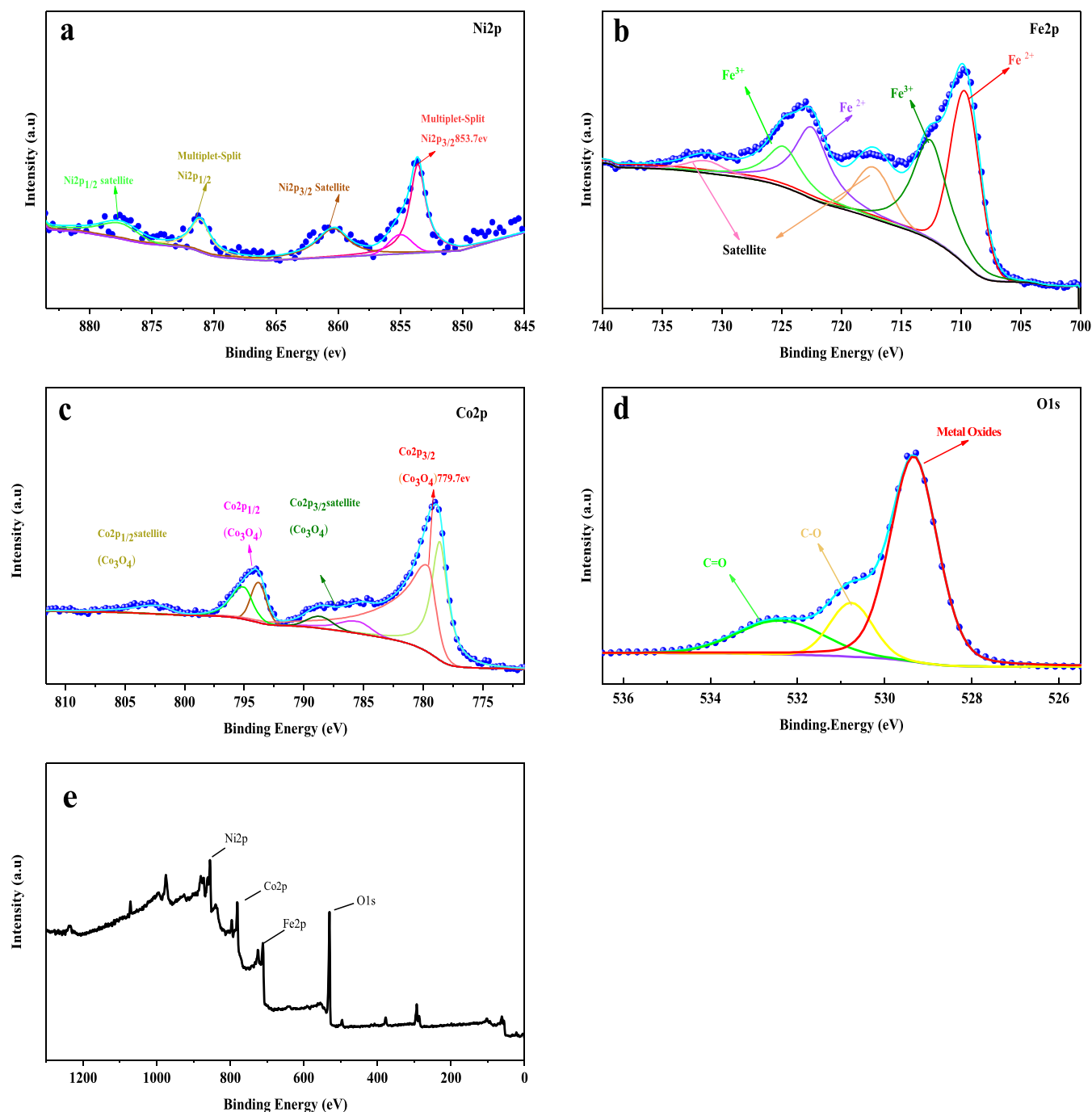
Figure 7. Full spectrum XPS spectrum of NFCO (a) Ni 2p, (b) Fe, (c) Co 2p, and (d) O 1s (e).

$$k = A e^{-E/RT} \tag{5}$$

Based on the dynamic test results, the model-free method can be used for thermodynamic analysis.[31] Among them, the Friedman method is the most common differential method, which is based on the principle of equal conversion, that is, the reaction rate at some constant conversion is only a function of temperature. When α = constant, $f(\alpha)$ is also constant.[32,33] Taking the logarithm of eq 3, the expression of the Friedman method can be obtained

$$\ln\left(\frac{d\alpha}{dt}\right)_{\alpha,i} = \ln[f(\alpha)A_\alpha] - \frac{E_\alpha}{RT_{\alpha,i}} \tag{6}$$

where i represents different temperature control methods, A refers to the front factor, R refers to the gas constant, E refers to the apparent activation energy, and $T_{\alpha,i}$ represents the temperature when the conversion α is reached under the ith temperature control method. For any given alpha value, the value of E_α can be obtained from the linear slope obtained by linear fitting of $\ln(d\alpha/dt)_{\alpha,i}$ and $1/T_{\alpha,i}$. Figure 10 shows the dynamic DSC test curves of different catalysts supported by NC.

Instrumental noise and baseline selection have a major impact on the curves during the reaction process, especially in the early and late phases. Therefore, in the analysis, only data within the range of 0.1 to 0.9 conversion rate (α) are
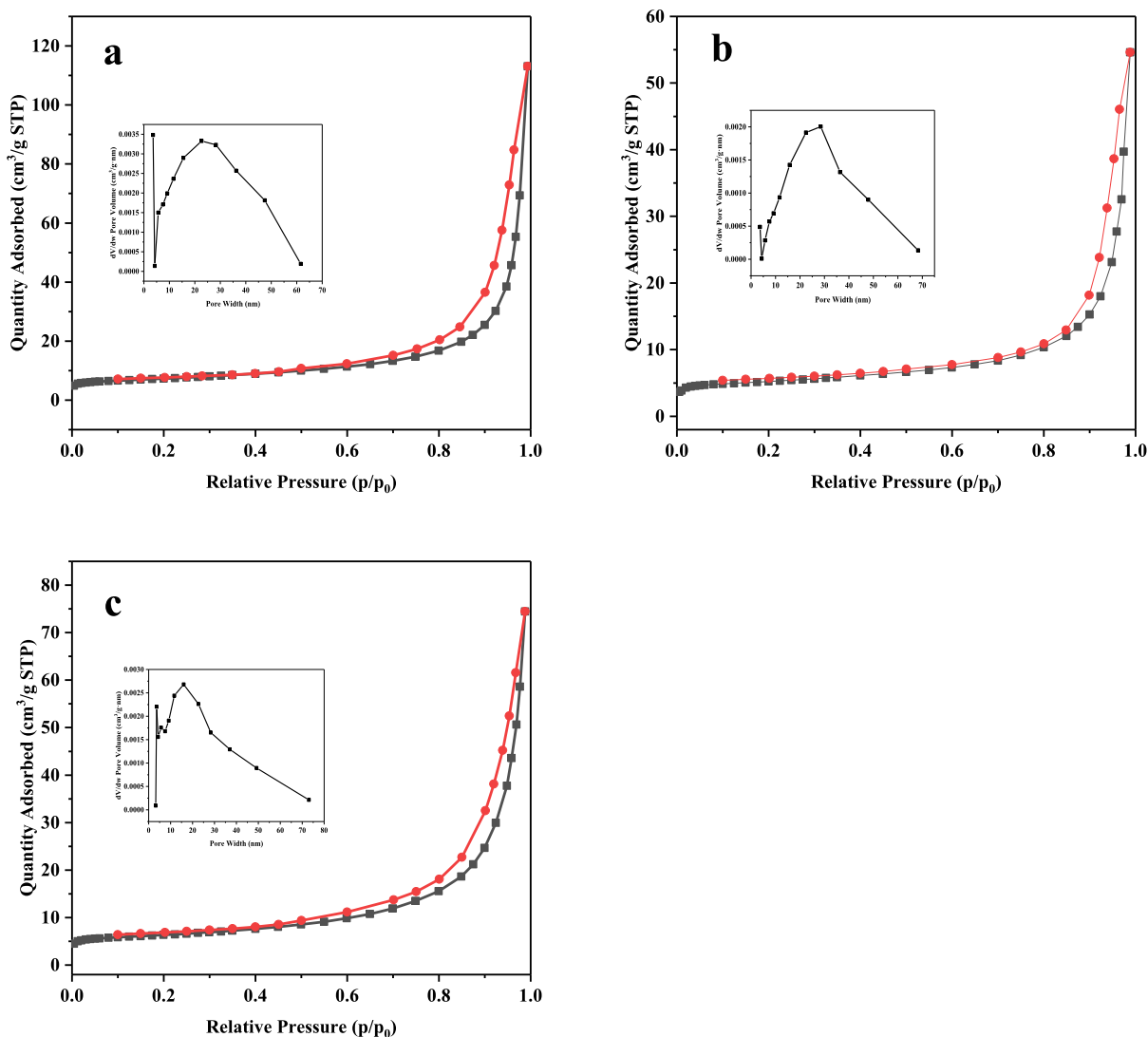
Figure 8. Nitrogen adsorption−desorption isotherms and pore size distribution plots of NFO, NCO, and NFCO.

Table 2. Structural Characteristics of the NFO, NCO, and NFCO Materials

samples	BET ($m^2 g^{-1}$)	pore volume ($cm^3 g^{-1}$)	pore size (nm)
NFO	26.40	0.18	24.22
NCO	19.63	0.085	26.16
NFCO	23.52	0.12	19.52

Table 3. Summary of Decomposition Parameters of NC and Different Catalyst Loads

	T_{onset} (°C)	T_p (°C)	T_f (°C)	Q (J/g)
NC	197.4	207.8	225.4	1629
NC + NFO	195.4	205.3	217.8	1650
NC + NCO	196.7	203.3	213.8	1697
NC + NFCO	196.9	202.5	210.6	1559

considered. In Figure 11, two regions of fluctuation in NC activation energy (E_a) are observed. During the thermal decomposition process of NC, E_a slowly increases from 180.29 to 201.04 kJ mol^{-1} in the range of $0.10 \leq \alpha \leq 0.80$ and then decreases from 201.04 to 176.96 kJ mol^{-1} in the range of $0.80 < \alpha \leq 0.90$. The overall average value of E_a throughout the process is 190.40 kJ mol^{-1}. However, after adding catalyst
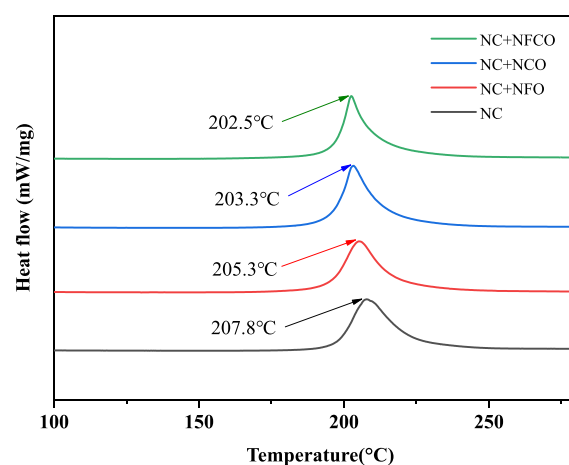

Figure 9. DSC curves of transition-metal oxide catalysts added to NC at 10 K/min NFO: Ni−Fe composite oxide; NCO: Ni−Co composite oxide; NFCO: Ni−Fe−Co composite oxide.

NFO, the activation energy still shows two regions of fluctuation. The first region appears within the range of $0.10 < \alpha < 0.43$, with E_a fluctuating between 193.80 and 212.04 kJ
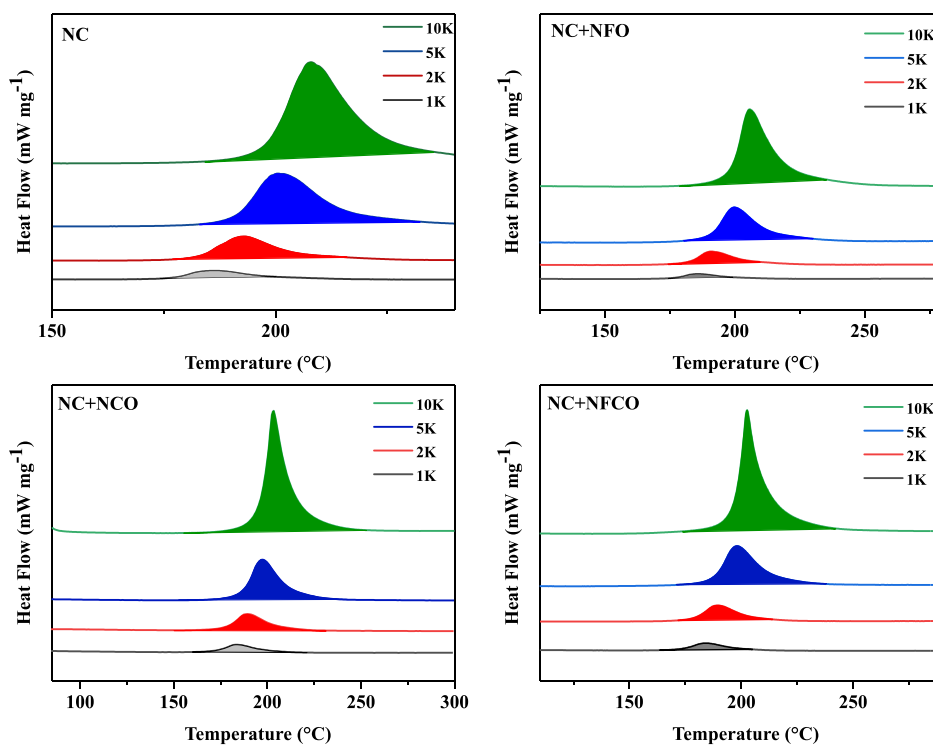
Figure 10. DSC curves of NC and NC with 20% NFO, NCO, and NFCO at different temperature rise rates.
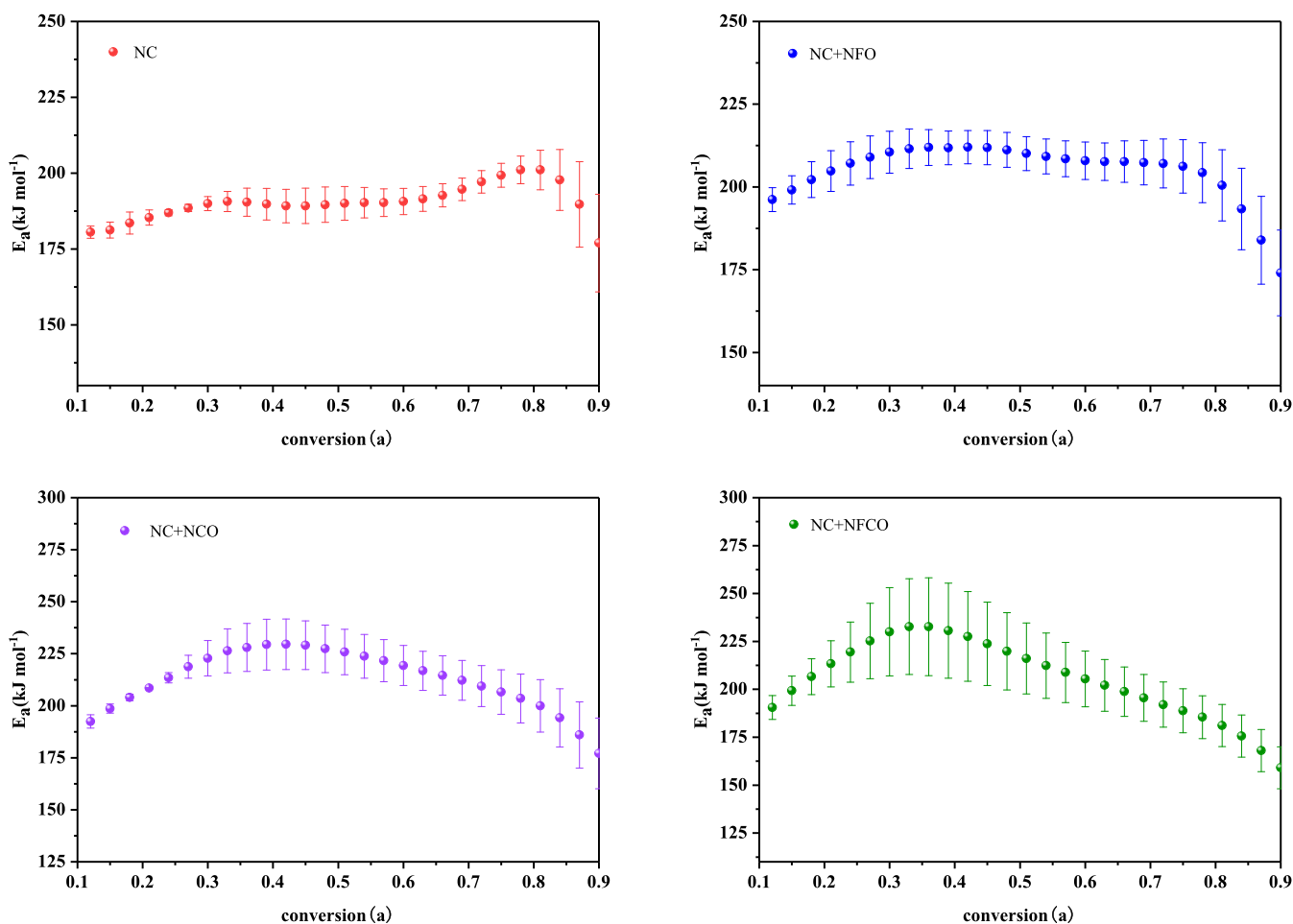

Figure 11. Activation energy curves of NC, NC + NFO, NC + NCO, and NC + NFCO are calculated by the Friedman method.

mol^{-1}. The second region appears within the range of $0.43 < \alpha < 0.90$, where E_a gradually decreases from 212.04 to 206.23 kJ mol^{-1} and then rapidly drops to 174.01 kJ mol^{-1}. The overall average E_a value is 204.97 kJ mol^{-1}.

Similarly, after adding catalyst NCO, the activation energy also exhibits two regions of fluctuation. The first region occurs within the range of $0.10 < \alpha < 0.40$, with E_a increasing from 188.21 to 229.67 kJ mol^{-1}. The second region appears within the range of $0.40 < \alpha < 0.90$, where E_a rapidly decreases from 229.67 to 177.10 kJ mol^{-1}. The overall average E_a value is 212.72 kJ mol^{-1}. Moreover, with the addition of catalyst NFCO, the activation energy continues to fluctuate in two regions. The first region appears within the range of $0.10 < \alpha < 0.35$, with Ea increasing from 183.91 to 232.97 kJ mol^{-1}. The second region occurs within the range of $0.35 < \alpha < 0.90$, where E_a rapidly decreases from 232.97 to 159.10 kJ mol^{-1}. The overall average E_a value is 205.53 kJ mol^{-1}. From the graph, it is evident that the activation energy curve shows significant fluctuations, and it is not straightforward to define NC's decomposition as a single-step reaction.[34]

The graph above makes it clear that adding catalysts has a big impact on NC's activation energy. In particular, there is a discernible difference in activation energy when NC is loaded with NFO, NCO, and NFCO within the range of $0.10 < \alpha < 0.40$. The maximum values of these values are 212.04, 229.67, and 232.97 kJ mol^{-1}, respectively, and they are noticeably higher than NC's activation energy of 201.43 kJ mol^{-1} at this point. In the second region, the overall trend is more consistent, but the sample with NFCO as the catalyst exhibits lower activation energy, with a minimum value of 159.10 kJ mol^{-1}. It can be inferred that for the first-step reaction, the addition of all three catalysts can increase the barrier for NC decomposition, and in the heat release, they are not substantial. The aforementioned dynamic DSC studies, however, demonstrate that the addition of catalyst will cause the decomposition temperature to advance and the reaction process to shorten, indicating that the decomposition will occur more quickly and that the specific heat difference will not be significant.

3.3.3. Dynamic Analysis Based on a Model Fitting Method. In order to determine certain reaction models and their kinetic parameters—which are assumed to reflect the connection between reaction rate and conversion—the model-fitting method was utilized.[35,36] Model fitting was used to examine the decomposition kinetics of NC and NC loaded with catalysts to precisely explain the decomposition process of NC and NC loaded with various catalysts. The reaction model of NC was examined using the generalized master plot method, as demonstrated in Figure 12. The first stage of NC's thermal decomposition process and the first step of NC's thermal decomposition process with additional catalysts are extremely compatible with the mechanism function C_{nm}. Furthermore, the mechanism function F_n is in excellent agreement with NC's second step and its thermal breakdown process when additional catalysts are applied. They subsequently established their kinetic models using a "model-based" methodology. Different kinetic models were chosen based on their close F-test result of 1, high R^2, and low S^2. The fitting curves and the experimental curves at 10 K min^{-1} are displayed in Figure 13, and the final kinetic model parameters are reported in the table.

Based on the previously mentioned reaction mechanism, a self-catalytic + Nth model was created for this study. The
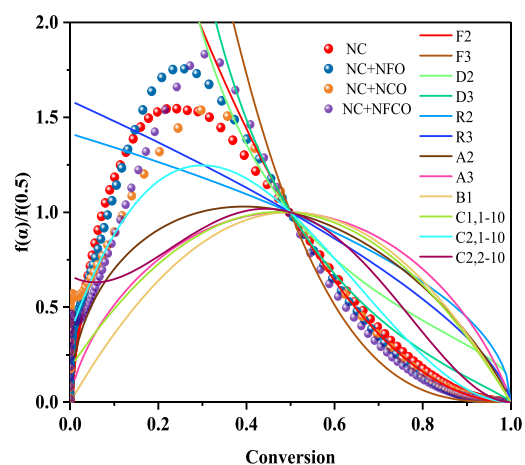

Figure 12. Experimental values and main diagram results established for each reaction type at a heating rate of 10 K min^{-1}.

model fitting results are shown in Figure 12, and the relevant kinetic parameters are shown in Table 4.

The two-step model constructed showed good agreement with the experimental curves. The kinetic model for the thermal decomposition of NC (Figure 13a) can be described as A → B→C. After adding the NFO catalyst (Figure 13b), the n-value for the nth-order reaction in the first step A → B increased from 1.07 to 1.46, with A and E_a values increasing from 1016.24 to 1018.24 (s^{-1}) and 177.13 to 187.38 (kJ mol^{-1}), respectively. The m-value in the m-order autocatalytic reaction increased from 0.83 to 1.56, while the contribution factor decreased from 0.40 to 0.27. Regarding the second step B → C, it can be noted that the kinetic model changed from C_{nm} to F_n. The n-value for the nth-order reaction increased from 2.09 to 2.78, with A and E_a values increasing from 1020.73 to 1027.31 (s^{-1}) and 206.76 to 264.14 (kJ mol^{-1}), respectively.

The n-value for the first step A−B reaction increased from 1.07 to 1.28 when the NCO catalyst was added (Figure 13c), whereas the values of A and Ea decreased from $10^{16.24}$ to $10^{15.44}$ (s^{-1}) and 177.13 to 160.31 (kJ mol^{-1}), respectively. While the contribution factor dropped from 0.40 to 0.27, the m-value in the m-order autocatalytic reaction rose from 0.83 to 1.56. Regarding the second step B → C, it can be noted that the kinetic model changed from C_{nm} to F_n. The n-value for the nth-order reaction increased from 2.09 to 3.22, with A and E_a values increasing from $10^{20.73}$ to $10^{36.68}$ (s^{-1}) and 206.76 to 346.14 (kJ mol^{-1}), respectively, indicating that adding NCO can promote the first step A → B.

After adding the NFCO catalyst (Figure 13d), the n-value for the nth-order reaction in the first step A → B increased from 1.07 to 1.32, with A and E_a values decreasing from $10^{16.24}$ to $10^{18.57}$ (s^{-1}) and 177.13 to 188.67 (kJ mol^{-1}), respectively. The m-value in the m-order autocatalytic reaction increased from 0.83 to 4.85, while the contribution factor increased from 0.40 to 0.55. Regarding the second step B → C, it can be noted that the kinetic model changed from C_{nm} to F_n. The n-value for the nth-order reaction increased from 2.09 to 5.25, with A and E_a values decreasing from $10^{20.73}$ to $10^{7.64}$ (s^{-1}) and 206.76 to 59.62 (kJ mol^{-1}).

4. CONCLUSIONS

In this study, PB analogues and their derivatives are prepared, and their effects on the performance of thermal degradation
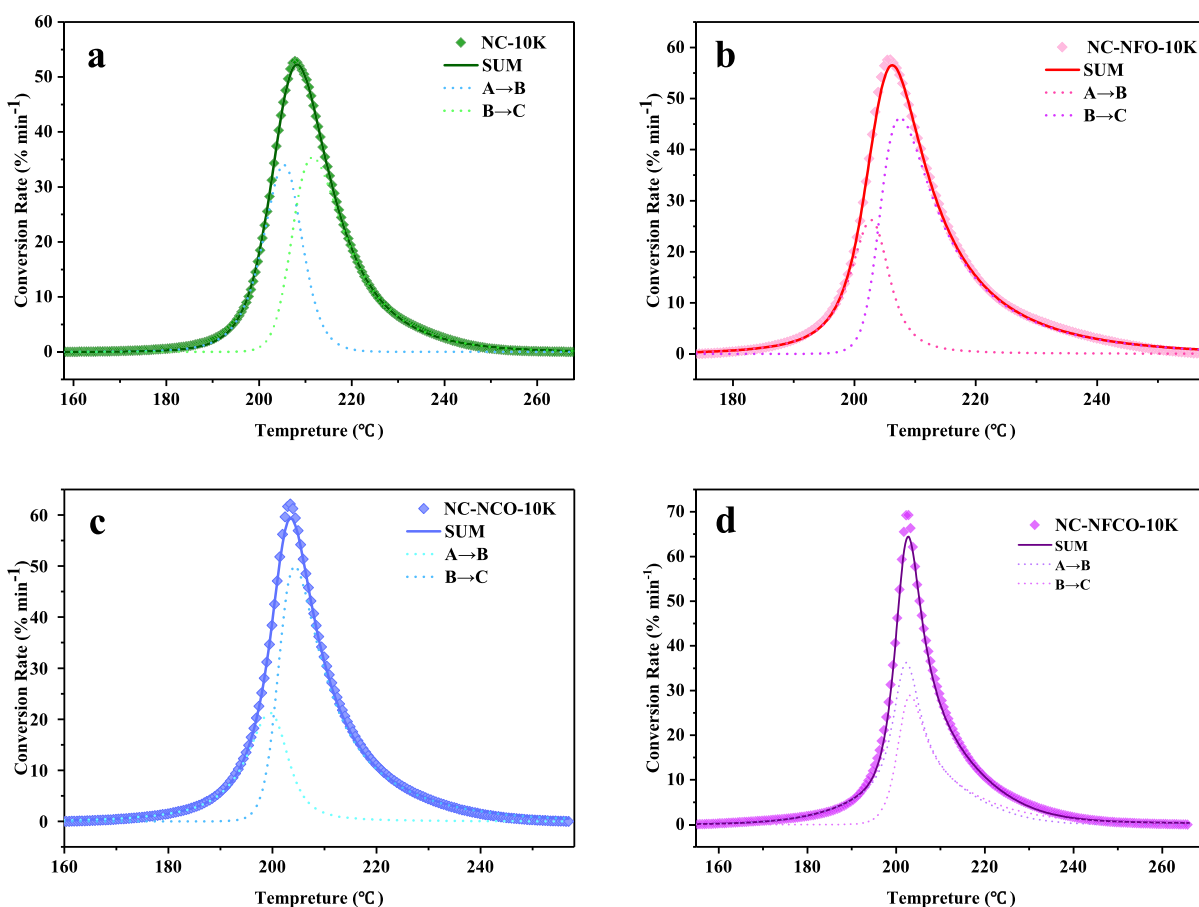
Figure 13. Kinetic models of NC (a), NC + NFO (b), NC + NCO (c), and NC + NFCO (d) compared with DSC curves at a heating rate of 10 K min^{-1}.

Table 4. Kinetic Model Parameters of Thermal Decomposition of NC, NC + NFO, NC + NCO, NC + NFCO

	NC	NC + NFO	NC + NCO	NC + NFCO
reaction type: C_{nm} step: A→ B				
equation: $\dfrac{d(a \rightarrow b)}{dt} = Aa^n(1 + \text{Autopreexp } b^m)\exp\left(-\dfrac{E_a}{RT}\right)$				
E_a/(kJ mol^{-1})	177.13	187.39	160.31	188.67
log$A$, A/S^{-1}	16.24	18.24	15.44	18.57
n	1.07	1.45	1.28	1.32
logAutocatpre exp, A/S^{-1}	1.87	1.46	1.24	3.236
autocat power m	0.83	1.56	1.56	4.85
contribution	0.40	0.27	0.27	0.55
reaction type: F_n step: B→ C				
equation: $\dfrac{d(b \rightarrow c)}{dt} = Ab^n\exp\left(-\dfrac{E_a}{RT}\right)$				
Ea/(kJ mol^{-1})	206.76	264.14	346.30	59.62
log$A$, A/S^{-1}	20.73	27.31	36.68	7.64
n	2.09	2.78	3.22	5.25
contribution	0.60	0.73	0.73	0.445

when added to NC are examined. The structural morphology and elemental composition of the PB analogues and their derivatives in porous nanocube composite materials were studied.

Through thermal decomposition experiments, it was found that PB derivatives have a significant influence on the thermal decomposition process of NC. After adding nanocomposite oxides, the peak temperatures were advanced by 3.9, 3.3, and 4.8 °C, and the termination temperatures were advanced by 7.6, 11.6, and 14.8 °C, respectively. Additionally, the decomposition temperature profiles were 28.0, 22.4, 17.1, and 13.7 °C. Moreover, the addition of nanocomposite oxides also led to an increase in activation energy to some extent. Particularly, when compared to the kinetic models of NC-NFO, NC-NCO, and NC-NFCO, the addition of NFO and NCO primarily affected the contribution factor and *m*-value (from 0.83 to 1.56) of the *m*-order autocatalytic reaction in the first step (A → B). The contribution factor also dropped from 0.40 to 0.27 at the same time. On the other hand, the introduction of NFCO had a more notable impact on NC, demonstrating a rise in the first step's rate of thermal decomposition contribution as well as a notable increase in the *m*-value and pre-exponential factor of the *m*-order autocatalytic process. Furthermore, considering the differences in contributing variables at each phase, it seems that the addition of NFO, NCO, and NFCO significantly altered the thermal degrading reaction of NC.

■ AUTHOR INFORMATION

Corresponding Author

Zhitao Liu − *School of Chemistry and Chemical Engineering, Nanjing University of Science and Technology, Nanjing, Jiangsu 210094, China;* ● orcid.org/0000-0001-6348-0417; Email: liuzhitao331@163.com

Authors

Junhong Liu − *School of Chemistry and Chemical Engineering, Nanjing University of Science and Technology, Nanjing, Jiangsu 210094, China;* ● orcid.org/0009-0002-0571-5198

Jing Yang − *School of Chemistry and Chemical Engineering, Nanjing University of Science and Technology, Nanjing, Jiangsu 210094, China*

Bin Xu − *School of Chemistry and Chemical Engineering, Nanjing University of Science and Technology, Nanjing, Jiangsu 210094, China*

Feiyun Chen − *School of Chemistry and Chemical Engineering, Nanjing University of Science and Technology, Nanjing, Jiangsu 210094, China*

Xin Liao − *School of Chemistry and Chemical Engineering, Nanjing University of Science and Technology, Nanjing, Jiangsu 210094, China*

Complete contact information is available at:
https://pubs.acs.org/10.1021/acsomega.3c08871

Notes

The authors declare no competing financial interest.

■ REFERENCES

(1) Mahajan, R. R.; Makashir, P. S.; Agrawal, J. P. Combustion behaviour of nitrocellulose and its complexes with copper oxide hot stage microscopic studies. *J. Therm. Anal. Calorim.* **2001**, *65* (3), 935−942.

(2) He, Y.; He, Y.; Liu, J.; Li, P.; Chen, M.; Wei, R.; Wang, J. Experimental study on the thermal decomposition and combustion characteristics of nitrocellulose with different alcohol humectants. *J. Hazard. Mater.* **2017**, *340*, 202−212.

(3) Zhang, X.; Hikal, W.; Zhang, Y.; Bhattacharia, S. K.; li, l.; Panditrao, S.; Wang, S.; Weeks, B. L. Direct laser initiation and improved thermal stability of nitrocellulose/graphene oxide nanocomposites. *Appl. Phys. Lett.* **2013**, *102*, 141905.

(4) Chelouche, S.; Trache, D.; Tarchoun, A. F.; Abdelaziz, A.; Khimeche, K.; Mezroua, A. Organic eutectic mixture as efficient stabilizer for nitrocellulose: Kinetic modeling and stability assessment. *Thermochim. Acta* **2019**, *673*, 78−91.

(5) Guo, P.-J.; Hu, R.-Z.; Ning, B.-K.; Yang, Z.-Q.; Song, J.-R.; Shi, Q.-Z.; Lu, G.-E.; Jiang, J.-Y. Kinetics of the First Order Autocatalytic Decomposition Reaction of Nitrocellulose (13.86% N). *Chin. J. Chem.* **2004**, *22* (1), 19−23.

(6) Bin, N. A Study on the Denitration Kinetics of Highly Nitrated Nitrocellulose, **2000**.

(7) Wei, W.; Cui, B.; Jiang, X.; Lu, L. The catalytic effect of NiO on thermal decomposition of nitrocellulose. *J. Therm. Anal. Calorim.* **2010**, *102* (3), 863−866.

(8) Quan, J.; Xu, E.; Zhu, H.; Chang, Y.; Zhu, Y.; Li, P.; Sun, Z.; Yu, D.; Jiang, Y. A Ni-doping-induced phase transition and electron evolution in cobalt hexacyanoferrate as a stable cathode for sodium-ion batteries. *Phys. Chem. Chem. Phys.* **2021**, *23* (3), 2491−2499.

(9) Soek, R. N.; Schmidt, A.; Winnischofer, H.; Vidotti, M. Anisotropic behavior of layer-by-layer films using highly disordered copper hexacyanoferrate(II) nanoparticles. *Appl. Surf. Sci.* **2016**, *378*, 253−258.

(10) Schoedel, A.; Li, M.; Li, D.; O'Keeffe, M.; Yaghi, O. M. Structures of Metal-Organic Frameworks with Rod Secondary Building Units. *Chem. Rev.* **2016**, *116* (19), 12466−12535.

(11) Decoste, J. B.; Peterson, G. W. Metal-Organic Frameworks for Air Purification of Toxic Chemicals. *Chem. Rev.* **2014**, *114* (11), 5695−5727.

(12) Huang, J.; Xu, P.; Gao, T.; Huangfu, J.; Wang, X.-J.; Liu, S.; Zhang, Y.; Song, B. Controlled Synthesis of Hollow Bimetallic Prussian Blue Analog for Conversion into Efficient Oxygen Evolution Electrocatalyst. *ACS Sustainable Chem. Eng.* **2020**, *8* (2), 1319−1328.

(13) Abebe, E. M.; Ujihara, M. Simultaneous Electrodeposition of Ternary Metal Oxide Nanocomposites for High-Efficiency Supercapacitor Applications. *ACS Omega* **2022**, *7* (20), 17161−17174.

(14) Wang, Y.; Pang, Z.; Xu, H.; Li, C.; Zhou, W.; Jiang, X.; Yu, L. High-performance electromagnetic wave absorption of NiCoFe/N-doped carbon composites with a Prussian blue analog (PBA) core at 2−18 GHz. *J. Colloid Interface Sci.* **2022**, *620*, 107−118.

(15) Peng, J.; Wang, J. S.; Yi, H. C.; Hu, W. J.; Yu, Y. H.; Yin, J. W.; Shen, Y.; Liu, Y.; Luo, J. H.; Xu, Y.; et al. A Dual-Insertion Type Sodium-Ion Full Cell Based on High-Quality Ternary-Metal Prussian Blue Analogs. *Adv. Energy Mater.* **2018**, *8* (11), 1702856.

(16) Song, K.; Pan, Y.-T.; Zhang, J.; Song, P.; He, J.; Wang, D.-Y.; Yang, R. Metal-Organic Frameworks-Based Flame-Retardant System for Epoxy Resin: A Review and Prospect. *Chem. Eng. J.* **2023**, *468*, 143653.

(17) Wang, L.; Zhang, X.; Li, C.; Xu, Y.; An, Y.; Liu, W.; Hu, T.; Yi, S.; Wang, K.; Sun, X.; et al. Cation-deficient T-Nb2O5/graphene Hybrids synthesized via chemical oxidative etching of MXene for advanced lithium-ion capacitors. *Chem. Eng. J.* **2023**, *468*, 143507.

(18) Zhao, Y.; Zhao, J. J.; Yao, Y. R.; Yang, Y. Fabrication of BSA@PB-P nanoparticles and their drug loading and controlled release of lamivudine. *New J. Chem.* **2023**, *47* (25), 11779−11783.

(19) Yin, Q. Y.; Cao, F. H.; Xu, T.; Han, B.; Liu, R. H.; Zeng, K. L.; Liu, R. M. Prussian blue analogues derived from NiFe-hydroxide nanoplates with synergistic effect and as high performance supercapacitors. *J. Alloys Compd.* **2023**, *960*, 170806.

(20) Liu, T.; Wang, J.; Jiang, Q.; Chai, N.; Ying, S. L.; Kong, Y. X.; Yi, F. Y. One-step synthesis of 2D@3D hollow Prussian blue analogue as a high-performance bifunctional electrochemical sensor. *Dalton Trans.* **2023**, *52* (26), 9048−9057.

(21) Tan, B.; Yang, X.; Dou, J.; Duan, B.; Lu, X.; Liu, N. Research progress on organic energetic burning rate catalysts for solid propellants. *Chin. J. Energetic Mater.* **2022**, *30* (8), 833−852.

(22) Ahn, W.; Park, M. G.; Lee, D. U.; Seo, M. H.; Jiang, G.; Cano, Z. P.; Hassan, F. M.; Chen, Z. Hollow multivoid nanocuboids derived from ternary ni-co-fe prussian blue analog for dual-electrocatalysis of oxygen and hydrogen evolution reactions. *Adv. Funct. Mater.* **2018**, *28*, 1802129.

(23) Li, Y.; Hu, J.; Yang, K.; Cao, B.; Li, Z.; Yang, L.; Pan, F. Synthetic control of Prussian blue derived nano-materials for energy storage and conversion application. *Mater. Today Energy* **2019**, *14*, 100332.

(24) Carvalho, C. L.; Silva, A. T.; Macedo, L. J.; Luz, R. A.; Neto, J.; Filho, U.; Cantanhede, W. New Hybrid Nanomaterial Based on Self-Assembly of Cyclodextrins and Cobalt Prussian Blue Analogue Nanocubes. *Int. J. Mol. Sci.* **2015**, *16* (12), 14594−14607.

(25) Xue, Z.; Li, L.; Cao, L.; Zheng, W.; Yang, W.; Yu, X. A simple method to fabricate NiFe2O4/NiO@Fe2O3 core-shelled nanocubes based on Prussian blue analogues for lithium ion battery. *J. Alloys Compd.* **2020**, *825*, 153966.

(26) Hu, M.; Belik, A. A.; Imura, M.; Mibu, K.; Tsujimoto, Y.; Yamauchi, Y. Synthesis of Superparamagnetic Nanoporous Iron Oxide Particles with Hollow Interiors by Using Prussian Blue Coordination Polymers. *Chem. Mater.* **2012**, *24* (14), 2698−2707.

(27) Zhang, L.; Wu, H. B.; Madhavi, S.; Hng, H. H.; Lou, X. W. Formation of Fe2O3 microboxes with hierarchical shell structures from metal-organic frameworks and their lithium storage properties. *J. Am. Chem. Soc.* **2012**, *134* (42), 17388−17391.

(28) Barman, B. K.; Nanda, K. K. Prussian blue as a single precursor for synthesis of Fe/Fe$_3$C encapsulated N-doped graphitic nanostructures as bi-functional catalysts. *Green Chem.* **2016**, *18* (2), 427−432.

(29) Liu, C.; Yuan, S.; Yang, Y.; Zhao, X.-X.; Duan, X.; Cao, B.; Wang, Q. Prussian blue analogues-derived nitrogen-doped carbon-coated FeO/CoO hollow nanocages as a high-performance anode material for Li storage. *Rare Met.* **2023**, *42* (12), 4070−4080.

(30) Ravi, P.; Gore, G. M.; Sikder, A. K.; Tewari, S. P. Thermal decomposition kinetics of 1-methyl-3,4,5-trinitropyrazole. *Thermochim. Acta* **2012**, *528*, 53−57.

(31) Sobek, S.; Werle, S. Kinetic modelling of waste wood devolatilization during pyrolysis based on thermogravimetric data and solar pyrolysis reactor performance. *Fuel* **2020**, *261*, 116459.

(32) Kameno, N.; Yamada, S.; Amimoto, T.; Amimoto, K.; Ikeda, H.; Koga, N. Thermal degradation of poly(lactic acid) oligomer: Reaction mechanism and multistep kinetic behavior. *Polym. Degrad. Stab.* **2016**, *134*, 284−295.

(33) Yang, F.; Liao, L.; Zhao, C.; Tian, Y. Combined kinetic analysis of overlapping multistep thermal decomposition of 5-nitro-2,4,6-triaminopyrimidine −1,3-di-N-oxide (ICM-102). *Thermochim. Acta* **2020**, *690*, 178663.

(34) Zhang, J.; Chen, L.; Zhao, L.; Jin, G.; He, W. Experimental insight into interaction mechanism of 1H-tetrazole and nitrocellulose by kinetics methods and TG-DSC-FTIR analysis. *J. Anal. Appl. Pyrolysis* **2023**, *169*, 105853.

(35) Cieślak, K.; Gańczyk-Specjalska, K.; Drożdżewska-Szymańska, K.; Uszyński, M. Effect of stabilizers and nitrogen content on thermal properties of nitrocellulose granules. *J. Therm. Anal. Calorim.* **2020**, *143*, 3459−3470.

(36) Vyazovkin, S. *Isoconversional Kinetics of Thermally Stimulated Processes*; Springer International Publishing, 2015..